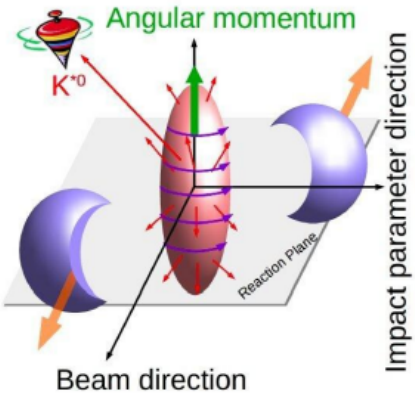
Rotating QCD Matter from Holography

Yidian Chen
Hangzhou Normal University

Collaborators Hiwa A. Ahmed, Ruixiang Chen, Xun Chen, Mei Huang, Danning Li and Zhibin Li

Papers in this talk
Phys. Rev. D **106**, 106002 (2022) Phys. Rev. D **111**, 046006 and 086006 (2025)
arXiv:2607.23199 and arXiv:2608.30930 (2026)

Angular Momentum in Noncentral Heavy-Ion Collisions



How does rotation change its phase structure? And how much of the spin alignment of vector mesons comes from the rotating matter?

STAR probes the fireball's vorticity through global hyperon polarization.

Diagram: Mohanty, ICTS News **6**(2), 18–20 (2020). STAR, Nature **548**, 62–65 (2017).

Outline

Introduction

Rotation in Holography

Spin Alignment

Summary

Outline

Introduction

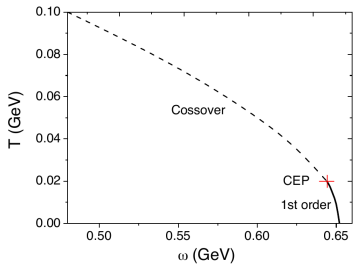
Rotation in Holography

Spin Alignment

Summary

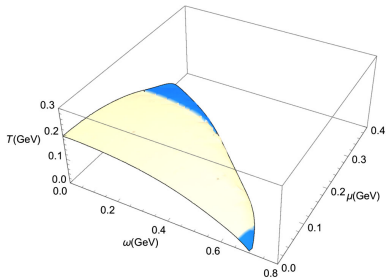
Rotating Chiral Phase Diagram in some Models

Zero chemical potential



The increasing the angular velocity lowers the chiral transition temperature. At large angular velocity, the model finds a first-order phase transition.

Phase surface in T, μ, ω

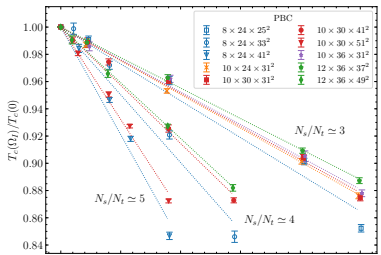


At $G_V = -0.5G_S$, blue marks first-order transitions and yellow marks crossover.

Jiang & Liao, Phys. Rev. Lett. **117**, 192302 (2016).
Wang, Wei, Li & Huang, Phys. Rev. D **99**, 016018 (2019).

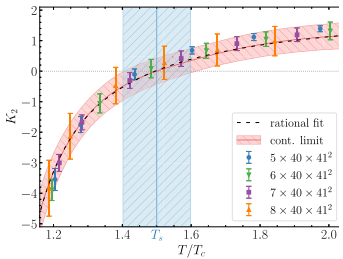
The Lattice Puzzle of the Rotating Phase Diagram

Pure-glue lattice QCD



The temperature goes down as the magnitude of imaginary rotation increases. Continuing the quadratic term to real angular velocity flips its sign and gives a rise at weak real rotation.

Negative inertia in gluon plasma



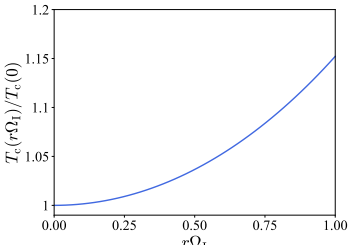
The moment of inertia is negative in the deconfined phase below about one and a half times the transition temperature.

How does the gluonic response to rotation affect the transition?

Braguta et al., Phys. Rev. D **103**, 094515 (2021); Braguta et al., Phys. Lett. B **852**, 138604 (2024).

Rotating Gluodynamics at Strong Coupling

Fukushima and Shimada



As the imaginary rotation increases, the transition temperature rises.

Wang, Chen, Hou and Ren

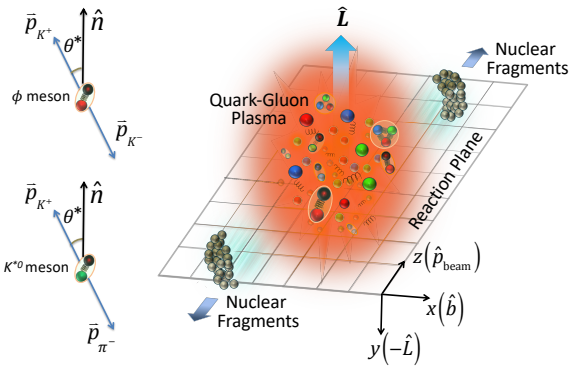
In the strong-coupling expansion, it was found that as the real rotation increases, the phase transition temperature decreases. Their formula connects the quadratic shift to the jump in moment of inertia and the latent heat at zero rotation.

$$\frac{T_c(\Omega)}{T_c(0)} = 1 - \frac{\Delta I}{2L}\Omega^2 + \mathcal{O}(\Omega^4).$$

Both strong-coupling trends differ from the numerical pure-glue lattice trend shown on the previous slide.

Fukushima & Shimada, Phys.Lett.B 868 (2025) 139716; Wang, Chen, Hou & Ren, arXiv:2505.15487.

Global Spin Alignment of Vector Mesons



STAR at RHIC

In Au–Au at 11.5–62 GeV, ϕ has $\rho_{00} > 1/3$. The K^{*0} measurement is consistent with the unpolarized value $1/3$.

ALICE at the LHC

In Pb–Pb at 2.76 TeV, $\rho_{00} < 1/3$ for both ϕ and K^{*0} at low p_{T}.

Open question

We'll come back to what rotation can explain.

STAR, Nature **614**, 244–248 (2023); ALICE, Phys. Rev. Lett. **125**, 012301 (2020).

Outline

Introduction

Rotation in Holography

Spin Alignment

Summary

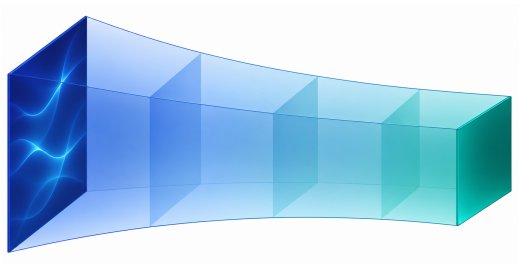
The Holographic Background

Boundary QCD

QCD lives on the four-dimensional boundary at $z = 0$.

Five-dimensional gravity

On the gravity side, we use an asymptotically AdS spacetime. The extra dimension tracks the renormalization group flow. We read off observables like the chiral condensate from the UV expansion of the bulk fields.



UV boundary $z = 0$ Black-brane horizon $z = z_h$

Schematic along the holographic direction z.

Three questions about rotation

How does rotation reshape the chiral condensate? How do the phase boundaries move when the gluonic background responds? What drives the anomalous moment of inertia in pure glue?

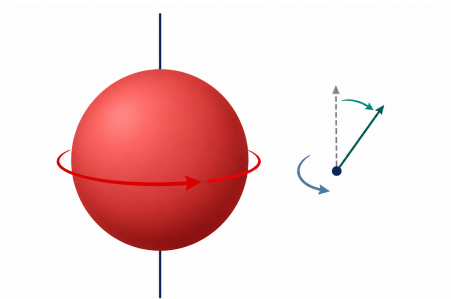
Frame Dragging as a Geometric Gauge Field

In the metric, the effect of rotation is to mix the temporal and spatial term. The mixed terms $2g_{ti}\,dt\,dx^i$ give a gravimagnetic connection A_i.

$$ds^2 = g_{tt}(dt + A_i\,dx^i)^2 + h_{ij}\,dx^i dx^j,$$
$$A_i = \frac{g_{ti}}{g_{tt}}.$$

Under $t \to t + \alpha(x)$, $A_i \to A_i - \partial_i\alpha$. In stationary, axisymmetric coordinates, the dragging rate is

$$\omega_{\mathrm{drag}} = \left.\frac{d\varphi}{dt}\right|_{p_\varphi=0} = -\frac{g_{t\varphi}}{g_{\varphi\varphi}} = -\frac{g_{tt}A_\varphi}{g_{\varphi\varphi}}.$$



Schematic analogy. A rotating sphere represents the QGP fireball. The arrows sharing one origin show a test spin at two orientations.

This geometric connection motivates a gauge-field description of rotation. The models below introduce effective bulk gauge sources.

Bardeen, Press & Teukolsky, Astrophys. J. **178**, 347 (1972).

The Rotating Soft-Wall Probe

On fixed AdS–Schwarzschild, use $D_M X = (\partial_M - iA_M)X$ with $f(z) = 1 - (z/z_h)^4$ and $L = 1$.

$$S_{\rm probe} = -\int d^5x\,\sqrt{-g}\,e^{-\Phi}\left\{\mathrm{Tr}\left[(D_M X)^\dagger D^M X + V_X(|X|)\right] + \tfrac{1}{4}F_{MN}F^{MN}\right\}.$$

The scalar $X = \chi\,\mathbf{1}/\sqrt{2N_f}$ is dual to the quark bilinear.

$$\chi(z,r) = m_q\zeta z + \cdots + \frac{\sigma(r)}{\zeta}z^3 + \cdots, \qquad A_\theta \;\leftrightarrow\; \bar{q}\gamma^\theta q, \qquad A_\theta(0,r) = \Omega(r)r^2.$$

At $\mu = 0$, the scalar and gauge field obey

$$\mathcal{D}_z^{(3)}\chi + (\partial_r^2 + r^{-1}\partial_r)\chi - \frac{V'(\chi)}{z^2} - \frac{A_\theta^2}{r^2}\chi = 0,$$

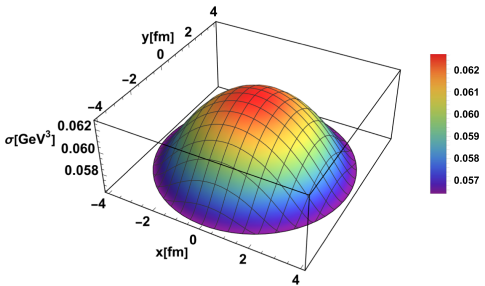
$$\mathcal{D}_z^{(1)}A_\theta + (\partial_r^2 - r^{-1}\partial_r)A_\theta - \frac{\chi^2}{z^2}A_\theta = 0, \qquad \mathcal{D}_z^{(n)} = z^n e^{\Phi}\partial_z\left(z^{-n}e^{-\Phi}f\,\partial_z\right).$$

$V(\chi) = \mathrm{Tr}\,V_X(|X|)$.

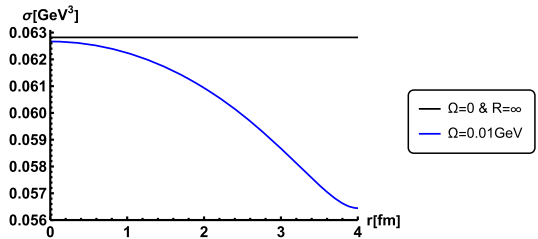
Chen, Li & Huang, Phys. Rev. D **106**, 106002 (2022).

Inhomogeneous Chiral Condensation under Rotation

Transverse surface $\sigma(x, y)$



Radial profile $\sigma(r)$

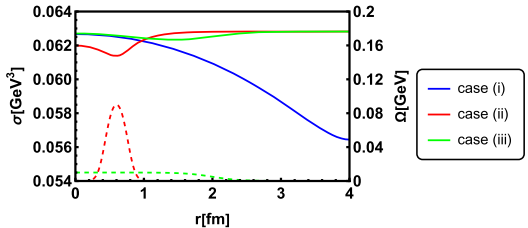


The condensate is largest at the center and decreases toward the edge, even though we imposed the same angular velocity throughout the cylinder. The black line is the nonrotating, infinite-volume reference.

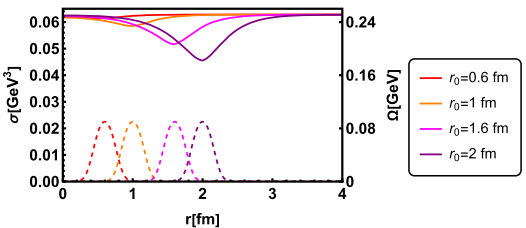
$\Omega = 0.01$ GeV, $R = 4$ fm.

Chen, Li & Huang, Phys. Rev. D **106**, 106002 (2022).

Chiral Condensation for Different Rotation Profiles



(a)

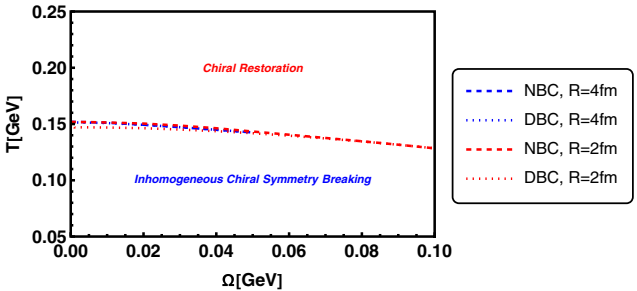


(b)

The dashed curves now show the imposed rotation, and the solid curves show the resulting condensate. Moving the peak of the vortex-like profile changes where the condensate is suppressed or enhanced. The chiral condensate is related to rotational linear velocity.
Neumann boundary condition.

Chen, Li & Huang, Phys. Rev. D **106**, 106002 (2022).

The Chiral Phase Diagram at Fixed Radius



Crossover criterion

Use the peak in the temperature slope magnitude of the central condensate at $m_q = 7$ MeV. For different radius and boundary conditions, the crossover temperature decreases with rotation.

What would happen if the gluon background also responded to the rotation?

Chen, Li & Huang, Phys. Rev. D **106**, 106002 (2022).

Anisotropic Einstein–Maxwell–Dilaton Background

The azimuthal gauge field now enters the background equations.

Einstein-frame action

$$S_G^e = \frac{1}{16\pi G_5}\int d^5x\,\sqrt{-g_e}\,\left[R_e - \tfrac{1}{2}(\partial\Phi)^2 - V_e(\Phi) - \tfrac{1}{4}h(\Phi)F_{MN}F^{MN}\right].$$

Near-axis geometry and gauge field

$$ds_e^2 = \frac{L^2 e^{2A_e(z)}}{z^2}\left[-f\,dt^2 + \frac{dz^2}{f} + e^B(dr^2 + r^2 d\theta^2) + e^{-2B}dx_3^2\right], \qquad A = A_t(z)\,dt + \Omega r^2\,d\theta.$$

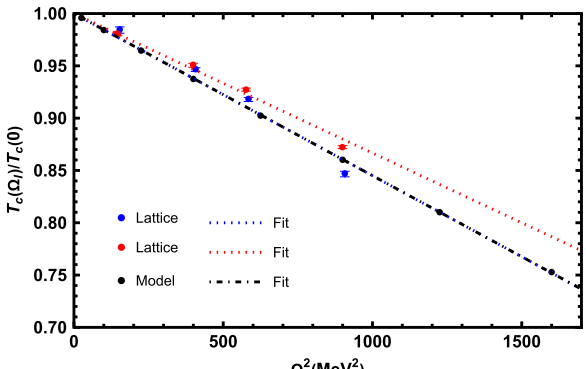
Rotation-dependent dilaton

$$\Phi(z;\Omega) = \bar{\mu}_G^2 z^2 \tanh\left(\frac{\mu_{G2}^4 z^2}{\bar{\mu}_G^2}\right), \qquad \bar{\mu}_G = \mu_G + \mu_\Omega \Omega^2.$$

The profile goes from $\mu_{G2}^4 z^4$ in the UV to $\bar{\mu}_G^2 z^2$ in the IR.

Chen et al., Phys. Rev. D **111**, 046006 (2025).

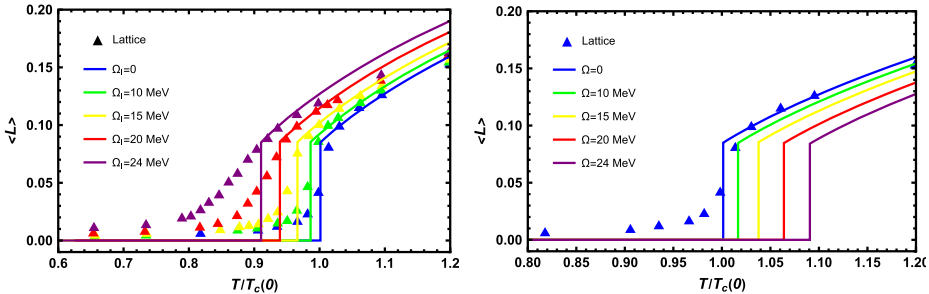
Calibrating the Imaginary-Rotation Response



The red and blue data points represent the numerical results of the pure gluon lattice simulations at different lattice sizes, respectively. We selected the black data points to fit the parameters. We then performed an analytical extension to real rotations and found that the deconfinement temperature shifts upward as a result.

Chen et al., Phys. Rev. D **111**, 046006 (2025).

Pure-Glue Deconfinement

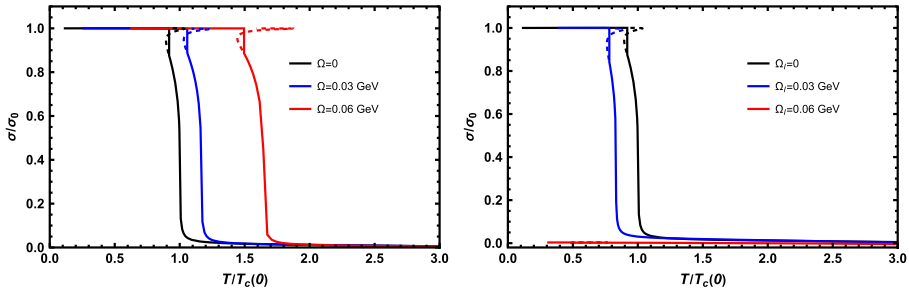


As the imaginary angular velocity increases, the transition temperature shifts toward lower temperatures. In real angular velocity calculations, the transition temperature shifts toward higher temperatures. The transition temperature increases as the real angular velocity increases, which is qualitatively consistent with the results of lattice QCD.

The loop normalization is calibrated at zero rotation.

Chen et al., Phys. Rev. D **111**, 046006 (2025).

Two-Flavor Chiral Restoration

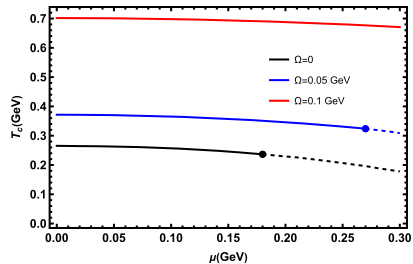


When the condensate is still relatively large, a small jump appears in the curve, which stems from a first-order phase transition in the background. The sharp drop in the condensation value identifies the chiral crossover point. Increasing the angular velocity will increase the temperature of the crossover.

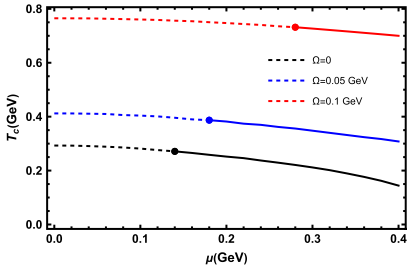
The background deconfinement transition can leave a sharp imprint on the probe.

Chen et al., Phys. Rev. D **111**, 046006 (2025).

Critical Endpoints at Finite Chemical Potential



(b)



(b)

From zero to an angular velocity of fifty MeV, both endpoints in this model move toward higher temperature and higher chemical potential.

Is it possible to realize a negative moment of inertia in the holographic model?

Chen et al., Phys. Rev. D **111**, 046006 (2025).

An EMD Model of Rotating Gluodynamics

Einstein-frame action

$$S = \frac{1}{2\kappa_5^2}\int d^5x\,\sqrt{-g}\left[\mathcal{R} - \tfrac{1}{2}(\partial\phi)^2 - V(\phi) - \tfrac{1}{4}Z(\phi)F_{MN}F^{MN}\right], \qquad Z(\phi) = \operatorname{sech}\!\left(\zeta\phi^3\right).$$

Anisotropic magnetic-brane geometry

$$ds^2 = -e^{-\eta(r)}f(r)\,dt^2 + \frac{dr^2}{f(r)} + r^2(dx^2+dy^2) + r^2 g(r)\,dz^2.$$

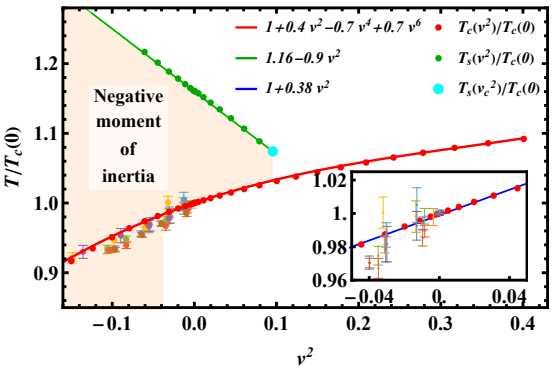
Here r is the bulk radial coordinate, and z is the rotation axis.

Rotation–magnetic correspondence

$$F_{xy} = B_{\text{eff}} = 2m(T)\Omega, \qquad m(T) = \lambda T, \qquad v = R\Omega.$$

Li, Chen & Huang, arXiv:2607.23199.

Calibration and the Deconfinement Line



The inset shows the small-velocity region.

Li, Chen & Huang, arXiv:2607.23199.

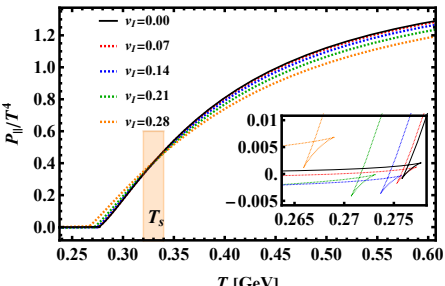
We use lattice data on that side to calibrate the mapping. The positive side gives the model prediction for real rotation. Close to zero, the slope of the normalized deconfinement temperature is about zero point three eight.

$$\frac{T_c(v^2)}{T_c(0)} \simeq 1 + 0.38 v^2 \quad (|v^2| \ll 1).$$

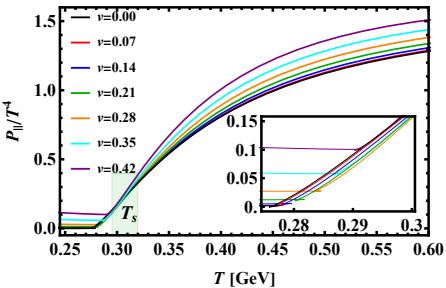
The larger-velocity curve contains higher-order contributions from the model.

Longitudinal Pressure under Rotation

Imaginary rotation



Real rotation

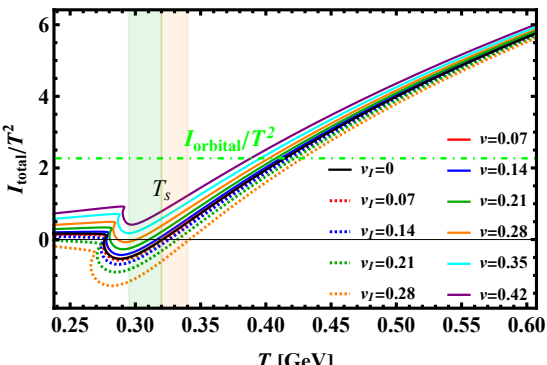


The point where the pressure curves in the two figures intersect is known as the supervortical temperature. Between the critical temperature and the supervortical temperature, the moment of inertia is negative.

The model gives $J_{\mathrm{tot}} = \partial P_{\parallel}/\partial\Omega$ at fixed T.

Li, Chen & Huang, arXiv:2607.23199.

The Negative Moment of Inertia



When the real rotation is weak, the moment of inertia falls slightly below zero above the deconfinement critical temperature, then rises again to zero at the temperature we call the supervortical temperature, T_s. When the angular velocity is sufficiently large, the total moment of inertia remains positive at all temperatures.

$$I_{\rm tot} = \frac{J_{\rm tot}}{\Omega} = I_{\rm orb} + I_{\rm spin}.$$

The horizontal green line indicates a positive orbital contribution.

Li, Chen & Huang, arXiv:2607.23199.

Outline

Introduction

Rotation in Holography

Spin Alignment

Summary

From In-Medium Spectra to Spin Alignment

Spin alignment

We work in the meson rest frame. Our spin axis is perpendicular to the event plane. ρ_{00} is the fraction of mesons with zero spin projection. Equal populations give $\rho_{00} = 1/3$.

From spectra to ρ_{00}

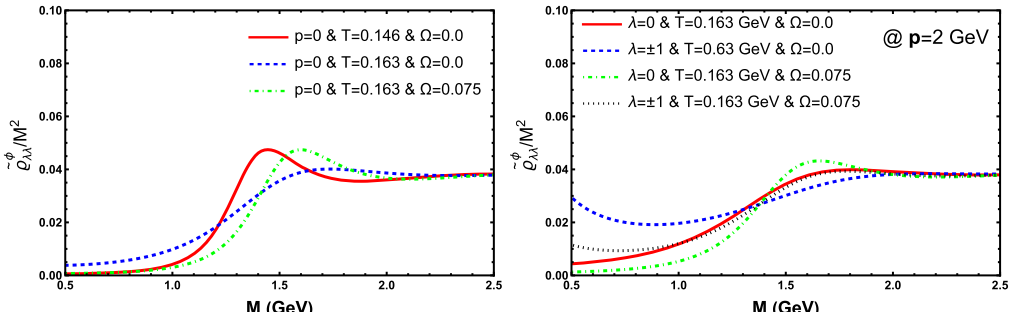
We use holography to calculate one spectrum per spin state. We assume freeze-out is instantaneous. The meson then propagates as in vacuum. For a narrow width, we read off the weights at the vacuum mass m_V. We divide the zero-projection weight by the total.

$$\rho_{00} \simeq \left. \frac{\widetilde{\varrho}_{00}}{\sum_{\lambda=0,\pm1} \widetilde{\varrho}_{\lambda\lambda}} \right|_{M=m_V} .$$

For the J/ψ comparison, we use $\lambda_\theta = (1 - 3\rho_{00})/(1 + \rho_{00})$.

Ahmed, Chen & Huang, Phys. Rev. D **111**, 086006 (2025); Chen et al., arXiv:2608.30930.

The ϕ Spectrum in a Rotating Medium

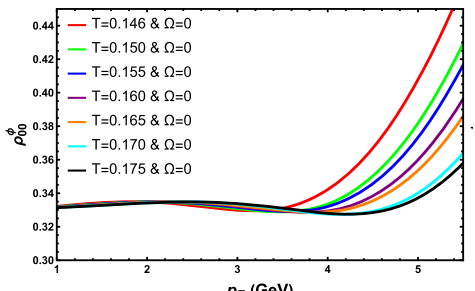


At $p = 0$, the peak disappears on heating to 163 MeV at $\Omega = 0$, and reappears there at $\Omega = 0.075$ GeV. At $p = 2$ GeV (right), the longitudinal and transverse spectral weights respond differently to rotation.

Ahmed, Chen & Huang, Phys. Rev. D **111**, 086006 (2025).

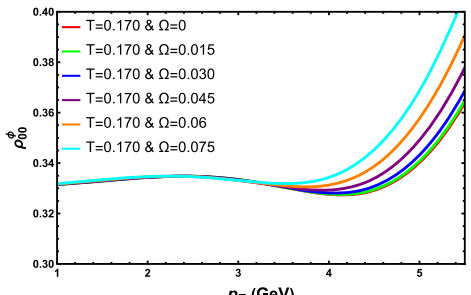
Temperature and Rotation Dependence of ϕ Spin Alignment

Varying T at $\Omega = 0$



Higher T lowers ρ_{00} at large p_{T}.

Varying Ω at $T = 170$ MeV

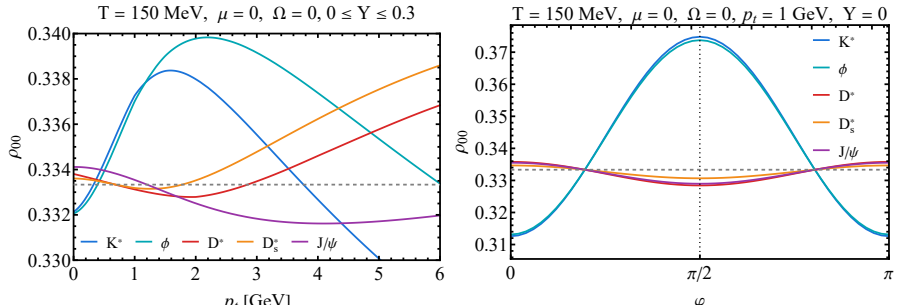


Faster rotation raises ρ_{00} at large p_{T}.

Both panels average over azimuth and use $|Y| \leq 0.75$.

Ahmed, Chen & Huang, Phys. Rev. D **111**, 086006 (2025).

Strange and Charm Mesons at Zero Rotation

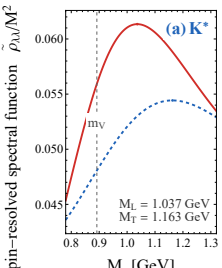


At low p_{T}, the four-flavor calculation gives $\bar{\rho}_{00} < 1/3$ for K^* and ϕ, and $\bar{\rho}_{00} > 1/3$ for D^*, D_s^*, and J/ψ. The right panel shows how the alignment varies with azimuth.
$T = 150$ MeV and $\mu = \Omega = 0$. The left panel also averages over $0 \leq Y \leq 0.3$.

Chen et al., arXiv:2608.30930.

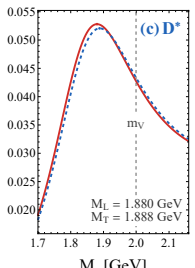
Why the Vacuum Mass Shell Matters

*K**



The vacuum mass lies below both thermal peaks. At $M = m_V$, the longitudinal weight is larger.

*D**

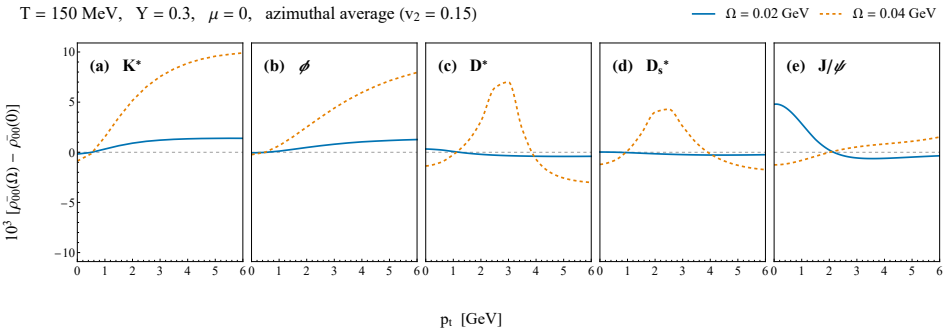


The vacuum mass lies above both thermal peaks. At $M = m_V$, the transverse weight is larger.

Fixed azimuth $\varphi = \pi/2$. Red solid: longitudinal. Blue dashed: transverse. $T = 150$ MeV, $\mu = \Omega = 0$, $Y = 0.3$, $p_T = 1$ GeV.

Chen et al., arXiv:2608.30930.

How Much Does Rotation Change the Alignment?

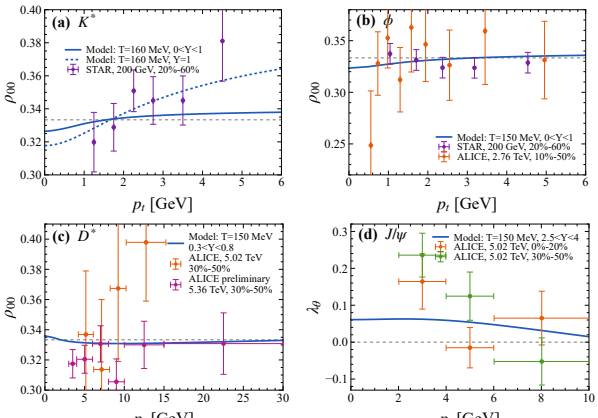


In the four-flavor calculation, the rotational shift is at most of order 10^{-2} in absolute $\bar{\rho}_{00}$ over the plotted range. Its sign and momentum dependence vary by meson.

$T = 150$ MeV, $Y = 0.3$, $\mu = 0$, $v_2 = 0.15$. Curves show $\Omega = 0.02$ and 0.04 GeV.

Chen et al., arXiv:2608.30930.

Equilibrium Spin Alignment Compared with Data



The J/ψ panel shows λ_θ. The D^* data at 5.36 TeV are preliminary.

Chen et al., arXiv:2608.30930.

The K star calculation gives a value below one third at low transverse momentum and then rises. That trend is qualitatively consistent with the STAR points at two hundred GeV. For the phi, the large enhancement reported by STAR at lower collision energies remains unexplained by this equilibrium calculation.

Outline

Introduction

Rotation in Holography

Spin Alignment

Summary

Conclusions

The transition depends on how rotation enters the dynamics

The finite-cylinder probe gives chiral suppression. The lattice-calibrated anisotropic backgrounds give a rising deconfinement temperature at weak real rotation.

Pure glue can have negative total inertia near deconfinement

In the rotation–magnetic model, the spin term can dominate the orbital term at weak real rotation. The negative-inertia window shrinks with increasing v^2.

Thermal spectral splitting produces flavor-dependent spin alignment

The vacuum mass shell samples different spectral weights for strange and charm mesons. Rotation makes a small additional correction in the 2026 calculation.

References

Holographic studies

Chen, Li & Huang, Phys. Rev. D **106**, 106002 (2022).
Chen et al., Phys. Rev. D **111**, 046006 (2025).
Li, Chen & Huang, arXiv:2607.23199.
Ahmed, Chen & Huang, Phys. Rev. D **111**, 086006 (2025).
Chen et al., arXiv:2608.30930.

Lattice benchmarks and measurements

Braguta et al., Phys. Rev. D **103**, 094515 (2021); Yang & Huang, arXiv:2307.05755.
Gupta et al., Phys. Rev. D **77**, 034503 (2008); Boyd et al., Nucl. Phys. B **469**, 419 (1996).
STAR, Nature **548**, 62 (2017) and **614**, 244 (2023). ALICE, Phys. Rev. Lett. **125**, 012301 (2020) and **131**, 042303 (2023); JHEP **09**, 094 (2025); ALI-PREL-633288.

Cylinder Equations and Boundary Data

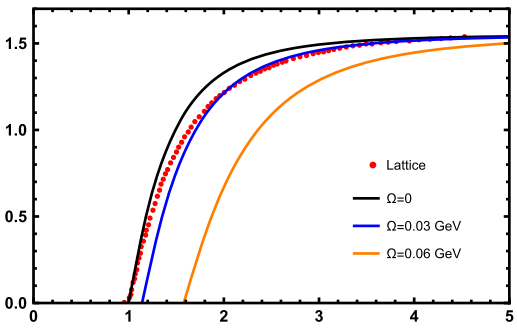
Write the chiral scalar near the UV boundary as $\chi(z,r) = m_q\zeta z + \cdots + \sigma(r)z^3/\zeta + \cdots$. At $\mu = 0$ the probe gauge equation is

$$\partial_z(f\partial_z A_\theta) - f(z^{-1} + \Phi')\partial_z A_\theta + \partial_r^2 A_\theta - r^{-1}\partial_r A_\theta - \chi^2 A_\theta = 0.$$

AdS boundary	$A_\theta(0,r) = \Omega(r)r^2$
Rotation axis	$A_\theta(z,0) = 0, \quad \partial_r\chi(z,0) = 0$
Outer wall	$A_\theta(z,R) = \Omega(R)R^2, \quad \partial_r\chi(z,R) = 0$ or $\chi(z,R) = 0$
Horizon	regular probe fields

Chen, Li & Huang, Phys. Rev. D **106**, 106002 (2022).

EMD Thermodynamics and Free Energy



Chen et al., Phys. Rev. D **111**, 046006 (2025).

The horizon gives $T = |f'(z_h)|/(4\pi)$ in the 2025 ansatz and s from the horizon area.

$$d\mathcal{F} = -s\,dT - \rho\,d\mu - j\,d\Omega.$$

At fixed μ, Ω, integrate the entropy to construct the free energy and compare branches.

Imaginary Rotation and Analytic Continuation

Fit the even expansion

$$\frac{T_c(\Omega)}{T_c(0)} = 1 + a_2\Omega^2 + a_4\Omega^4 + \cdots, \qquad \frac{T_c(i\Omega_I)}{T_c(0)} = 1 - a_2\Omega_I^2 + a_4\Omega_I^4 + \cdots.$$

- In the anisotropic model, the imaginary-rotation slope fixes the phenomenological dilaton shift.
- In the pure-glue magnetic correspondence, the low-$|v^2|$ data calibrate the conversion factor λ.
- The quadratic trend is local to small rotation. At larger real v^2, the pure-glue model resolves higher-order corrections.

Chen et al., Phys. Rev. D **111**, 046006 (2025); Li, Chen & Huang, arXiv:2607.23199.

Inertia from the Stress Anisotropy

The pure-glue dictionary uses $P_{\parallel} - P_{\perp} = \Omega J_{\mathrm{tot}}$, so that for $\Omega \neq 0$,

$$I_{\mathrm{tot}} = \frac{P_{\parallel} - P_{\perp}}{\Omega^2} = \underbrace{\frac{m^2 Z(0)}{2\kappa_5^2}}_{I_{\mathrm{orb}}} + \underbrace{\frac{4 g_v}{2\kappa_5^2 g_0 \Omega^2}}_{I_{\mathrm{spin}}}.$$

g_0 is the boundary value of the metric anisotropy and g_v is its normalizable coefficient. The second term encodes the medium response in the authors' spin interpretation.

Li, Chen & Huang, arXiv:2607.23199.

Spectral Projection and Instantaneous Freeze-Out

At fixed momentum the spin-resolved yield is an integral over the spectral rate. For a narrow vacuum width the rate samples $M \simeq m_V$.

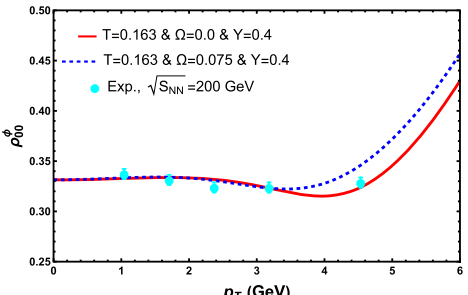
$$\rho_{00} = \frac{\int d\omega\, n_0}{\sum_\lambda \int d\omega\, n_\lambda} \simeq \left. \frac{\widetilde{\varrho}_{00}}{\sum_\lambda \widetilde{\varrho}_{\lambda\lambda}} \right|_{M=m_V}.$$

In the 2026 calculation the event-plane azimuthal average uses the normalized weight proportional to $1 + 2v_2 \cos(2\varphi)$, with $v_2 = 0.15$.

Chen et al., arXiv:2608.30930.

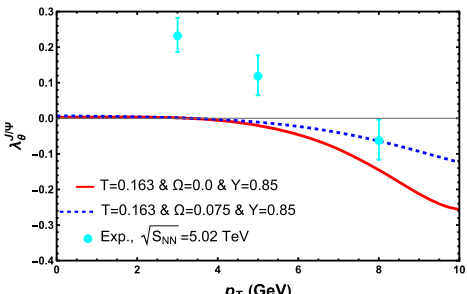
ϕ and J/ψ Spin Alignment Compared with Data

ϕ ρ_{00} and STAR data



Au–Au at $\sqrt{s_{NN}} = 200$ GeV. The model uses $Y = 0.4$.

J/ψ λ_θ and ALICE data

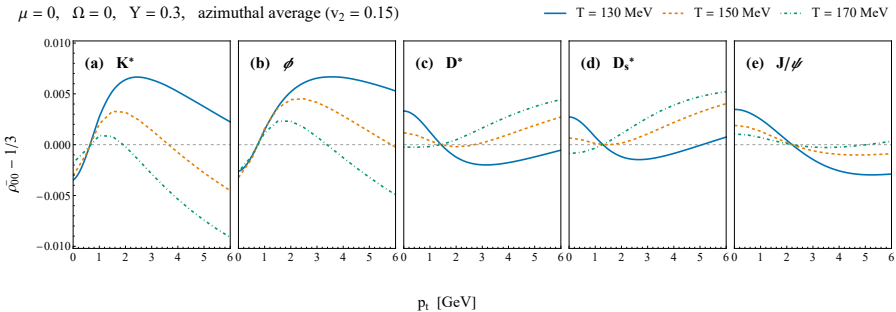


Pb–Pb at $\sqrt{s_{NN}} = 5.02$ TeV. The data cover $2.5 < Y < 4$, and the model uses $Y = 0.85$.

Model curves use $T = 163$ MeV and $\Omega = 0$ (solid) or 0.075 GeV (dashed).

Ahmed, Chen & Huang, Phys. Rev. D **111**, 086006 (2025).

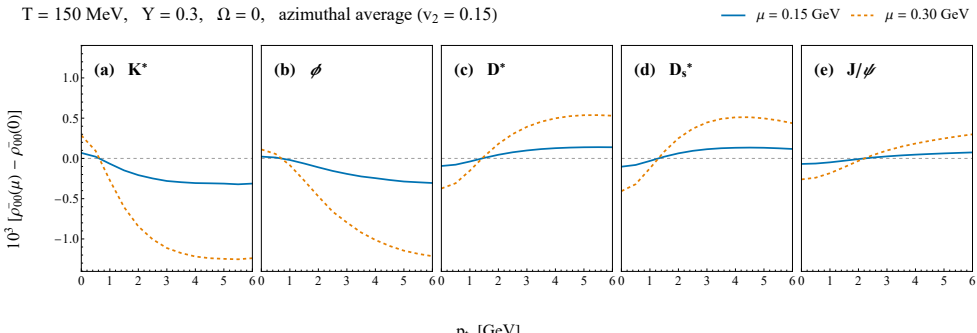
Temperature Dependence of $\bar{\rho}_{00}$



Between 130 and 170 MeV, changing the temperature reshapes the momentum dependence. The size and sign of the change depend on the meson and p_{T}.
$Y = 0.3$, $\mu = \Omega = 0$. The azimuthal average uses $v_2 = 0.15$.

Chen et al., arXiv:2608.30930.

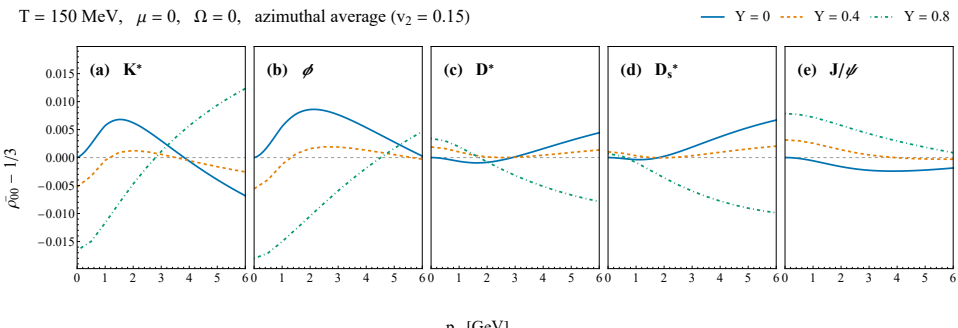
Chemical-Potential Dependence of $\bar{\rho}_{00}$



Changing the baryon chemical potential shifts $\bar{\rho}_{00}$ by about 10^{-3} or less in most of the plotted range. At $\mu = 0.30$ GeV and high p_{T}, the shift is negative for K^* and ϕ, and positive for D^* and D_s^*.

Chen et al., arXiv:2608.30930.

Rapidity Dependence of $\bar{\rho}_{00}$



The rapidity dependence varies across flavors and momentum. For K^* and ϕ, increasing Y lowers $\bar{\rho}_{00}$ at low p_T and raises it at high p_T in the kinematics shown.

Chen et al., arXiv:2608.30930.

Kinematic Windows for the Data Comparison

$\mu = \Omega = 0$ for the equilibrium curves.

Meson	Model window	Measurements
K^*	160 MeV, $0 < Y < 1$ and $Y = 1$	STAR Au–Au, 200 GeV
ϕ	150 MeV, $0 < Y < 1$	STAR 200 GeV; ALICE 2.76 TeV
D^*	150 MeV, $0.3 < Y < 0.8$	ALICE Pb–Pb, 5.02 and 5.36 TeV
J/ψ	150 MeV, $2.5 < Y < 4$	ALICE Pb–Pb, 5.02 TeV, λ_θ

The plot legends give the experimental centrality ranges. The ALICE D^* points at 5.36 TeV are preliminary (ALI-PREL-633288).

Chen et al., arXiv:2608.30930.